iScience

CellPress
OPEN ACCESS

Article

Macrophage ferroportin serves as a therapeutic target against bacteria-induced acute lung injury by promoting barrier restoration

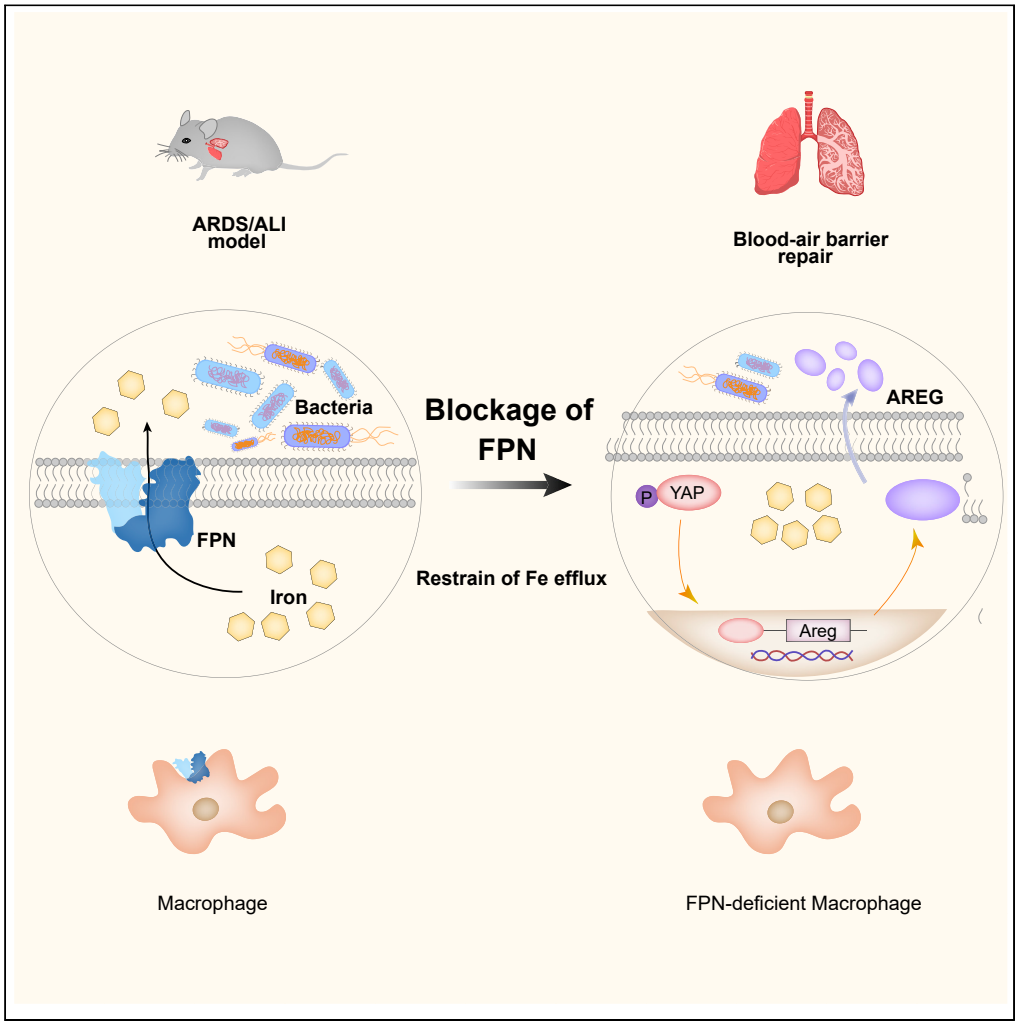

Hanbin Wang, Congli Zeng, Gan Luo, ..., Kai Zhang, Marcos F. Vidal Melo, Xiangming Fang

xmfang@zju.edu.cn

Highlights

Macrophage FPN is a risk factor in ARDS patients because of bacterial pneumonia

Loss of macrophage FPN reduces susceptibility to bacteria-induced ALI mice

FPN deficiency in macrophages preserves the lung barrier integrity by upregulating Areg

A redesigned hepcidin protect against bacterial-induced ALI mice by degrading FPN

Wang et al., iScience 25, 105698
December 22, 2022
https://doi.org/10.1016/j.isci.2022.105698

iScience

CellPress
OPEN ACCESS

Article

Macrophage ferroportin serves as a therapeutic target against bacteria-induced acute lung injury by promoting barrier restoration

Hanbin Wang,[1,4] Congli Zeng,[2,4] Gan Luo,[1,4] Yaqi Sun,[1] Jue Zhang,[1] Zhipeng Xu,[1] Yuqian Guo,[1] Hui Ye,[1] Jiali Mao,[1] Shiyu Chen,[1] Yan Zhang,[3] Kai Zhang,[1] Marcos F. Vidal Melo,[2] and Xiangming Fang[1,4,5,*]

SUMMARY

Acute respiratory distress syndrome (ARDS) is a common lung disorder that involves severe inflammatory damage in the pulmonary barrier, but the underlying mechanisms remain elusive. Here, we demonstrated that pulmonary macrophages originating from ARDS patients and mice caused by bacteria were characterized by increased expression of ferroportin (FPN). Specifically deleting FPN in myeloid cells conferred significant resistance to bacterial infection with improved survival by decreasing extracellular bacterial growth and preserving pulmonary barrier integrity in mice. Mechanistically, macrophage FPN deficiency not only limited the availability of iron to bacteria, but also promoted tissue restoration via growth factor amphiregulin, which is regulated by cellular iron-activated Yes-associated protein signaling. Furthermore, pharmacological treatment with C-Hep, the self-assembled N-terminally cholesterylated minihepcidin that functions in the degradation of macrophage FPN, protected against bacteria-induced lung injury. Therefore, therapeutic strategies targeting the hepcidin-FPN axis in macrophages may be promising for the clinical treatment of acute lung injury.

INTRODUCTION

Acute respiratory distress syndrome (ARDS) is a common and severe lung disorder. It is characterized by acute and diffuse inflammatory damage to the alveolar-capillary barrier and is associated with increased permeability, leading to subsequent alveolar flooding with protein rich fluid and impairment of gas exchange.[1,2] Despite decades of research, ARDS remains a condition with high mortality and exhibits no effective pharmacological therapies. Bacterial infection has been recognized as a major underlying cause of ARDS.[3] As an essential effector cell of pulmonary defense against foreign stimuli, macrophages play a critical role in the pathophysiology and development of lung injury following infection.

Ferroportin (FPN), the sole known cellular iron exporter, is expressed on the surface of macrophages. It can be internalized and degraded by binding its ligand hepcidin, a principal iron regulatory hormone mainly produced by hepatocytes. Accordingly, the degradation of FPN by hepcidin promotes cellular iron sequestration in macrophages, which subsequently limits extracellular bacterial infection.[4,5] In addition to the liver, hepcidin has also been documented in airway epithelial cells.[6] Recently, experimental studies have indicated that macrophage FPN might be involved in the protective effects against murine lung injury because of locally produced hepcidin by airway epithelial cells.[7,8] However, the exact role and potential mechanism of macrophage FPN during acute lung injury remains unclear.

In this study, we examined the expression of FPN in pulmonary macrophages from ARDS patients caused by bacterial pneumonia and analyzed its relationship with pulmonary oxygenation and clinical complications. We next constructed a clinically relevant bacteria-induced lung injury model by using mice with myeloid-specific deletion of FPN ($Fpn^{LysM/LysM}$). We observed the exact role, the key molecule and the underlying mechanism of macrophage FPN during lung injury. Finally, we investigated the potential therapeutic efficacy of the hepcidin-FPN axis by assessing the treatment with C-hepcidin (C-Hep, self-assembled cholesterylated minihepcidin) in limiting pulmonary barrier damage and lung injury.

[1]Department of Anesthesiology and Intensive Care, The First Affiliated Hospital, School of Medicine, Zhejiang University, Hangzhou 310003, China

[2]Department of Anesthesiology, Vagelos College of Physicians and Surgeons, Columbia University, New York, NY 10032, USA

[3]National Clinical Research Center for Child Health, Children's Hospital, School of Medicine, Zhejiang University, Hangzhou 310052, China

[4]These authors contributed equally

[5]Lead contact

*Correspondence: xmfang@zju.edu.cn

https://doi.org/10.1016/j.isci.2022.105698

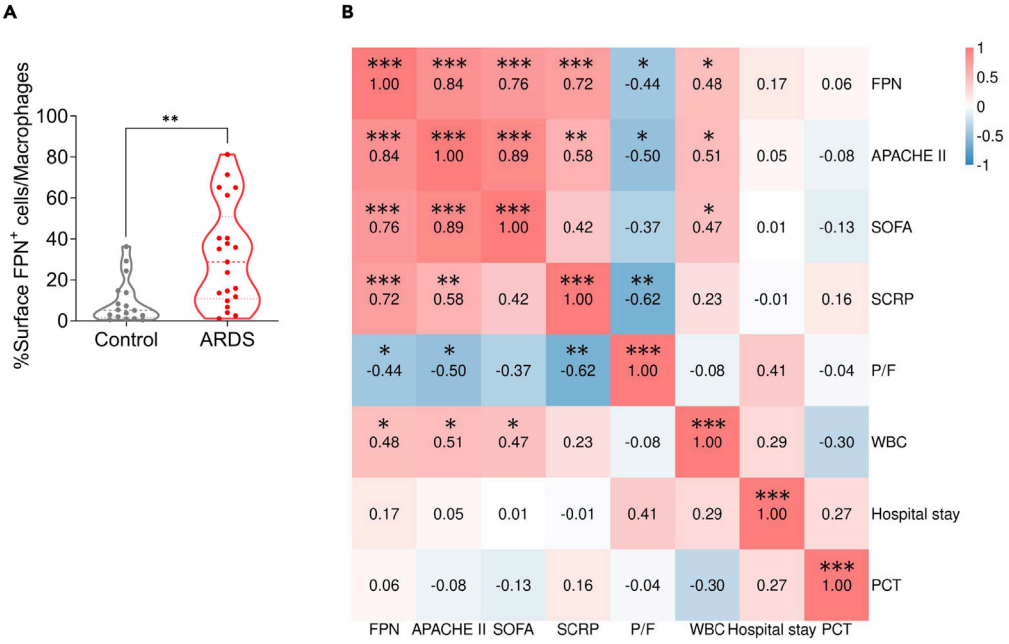

Figure 1. Macrophage FPN is a risk factor in ARDS patients with bacterial pneumonia

(A) FPN levels in pulmonary macrophages were measured by flow cytometry in controls (n = 17) and ARDS patients (n = 21). (B) Correlations of FPN levels, SCRP, SOFA, APACHE II, P/F, WBC, Hospital stay and PCT were assessed with pearson. Clustering correlation heatmap with signs was performed using the OmicStudio tools at https://www.omicstudio.cn. All data are representative of at least two independent experiments (mean ± SEM). For comparison between two experimental groups, unpaired two-tailed Student's t-test or nonparametric test was performed. *p< 0.05; **p< 0.01; ***p< 0.001. FPN = ferroportin; SCRP = supersensitive C-reactive protein; SOFA = sequential organ failure assessment; APACHE II = acute physiology and chronic health evaluation; P/F = PaO_2/FiO_2; WBC = white blood cell; PCT = procalcitonin.

RESULTS

Macrophage FPN is a risk factor in ARDS patients with bacterial pneumonia

To uncover the potential roles of pulmonary macrophage FPN in the ARDS pathogenesis, controls and ARDS patients with bacterial pneumonia were enrolled, and the expression of FPN in pulmonary macrophages was measured by flow cytometry. The demographic and clinical characteristics of the subjects are listed in online Table S1. Compared with the controls, the percentages of FPN-positive pulmonary macrophages dramatically increased in ARDS patients with bacterial pneumonia (Figure 1A). Moreover, such percentages were negatively correlated with the oxygenation index but positively correlated with the Acute Physiology and Chronic Health Enquiry (APACHE II) score and serum C-reactive protein levels of ARDS patients (Figure 1B), indicating the clinical roles of macrophage FPN in ARDS pathogenesis.

FPN deficiency in macrophages reduces susceptibility to bacteria-induced acute lung injury

We next examined the expression of FPN in macrophages from two models of bacteria-induced lung injury. Parallel to clinical findings, FPN was significantly upregulated in mouse primary pulmonary macrophages at 12 h post bacterial challenge (Figures 2A and S1). We thus explored the physiological role of macrophage FPN in acute lung injury using mice that lacked FPN in the myeloid lineage ($Fpn^{LysM/LysM}$) by crossing $Fpn^{flox/flox}$ mice with Cre recombinase mice, which were under the control of the lysozyme M (LysM) promoter. The results demonstrated that the survival rates of $Fpn^{LysM/LysM}$ mice with acute lung injury caused by *Escherichia coli* (*E. coli*) or *Klebsiella pneumoniae* (*K. pneumoniae*) were significantly improved (Figures 2B and 2C). Correspondingly, attenuation of histopathological lung injury was observed in $Fpn^{LysM/LysM}$ mice after bacterial infection (Figure 2D). Furthermore, less disruption of lung barrier integrity from $Fpn^{LysM/LysM}$ mice relative to $Fpn^{flox/flox}$ mice was also verified by the Evans blue dye assay (Figure 2E). In addition, the proinflammatory cascades in $Fpn^{LysM/LysM}$ mice were significantly diminished, as indicated by the relatively low expression levels of IL-1β and TNF-α in bronchoalveolar lavage fluid (BALF) (Figure S2). The beneficial effects of FPN knockout were further supported by markers of alveolar-capillary barrier

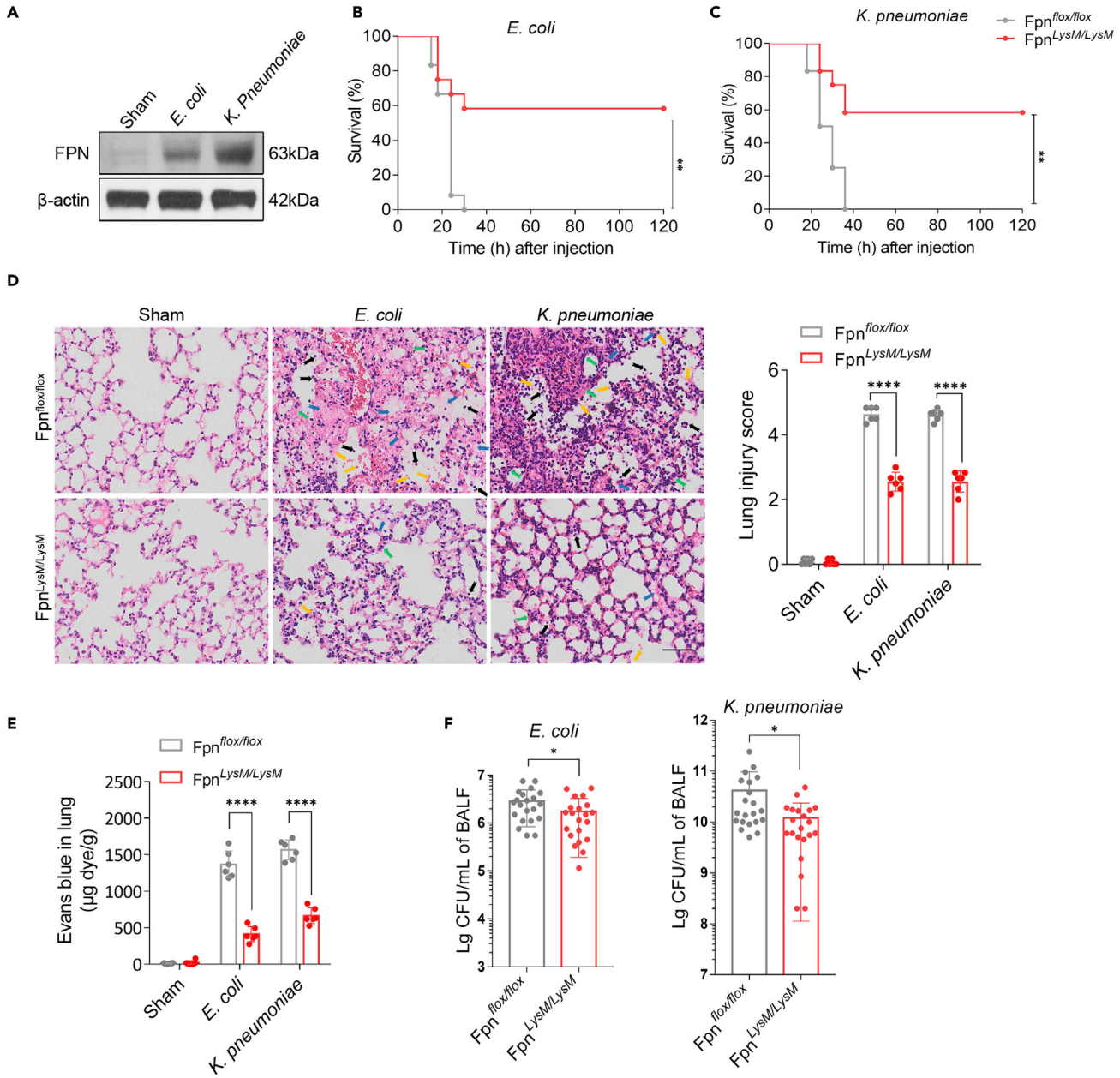

Figure 2. FPN deficiency in macrophages reduces susceptibility to bacteria-induced acute lung injury

$Fpn^{LysM/LysM}$ and $Fpn^{flox/flox}$ mice were subjected to *E coli* or *K. pneumoniae*-induced acute lung injury.

(A) Protein levels of FPN were increased in primary pulmonary macrophages exposed to saline control, *E. coli* or *K. pneumoniae* for 12 h (n = 3 per group). β-Actin served as an internal control.

(B and C) Survival was monitored during *E. coli* (B) or *K. pneumoniae* (C) infection (n = 12 per group, from 3 independent experiments with 4 mice for each experiment).

(D) Representative images of lungs with hematoxylin and eosin staining and quantification of lung injury score at 24 h (n = 6 per group, from 3 independent experiments; scale bar, 100 μm). Histologic image showing the inflammatory cells infiltration (black arrows), fibrin deposits (blue arrows) and erythrocyte (yellow arrows) in the airspace and alveolar septal thickening (green arrows).

(E) *In vivo* Evans blue dye permeability assay in lungs at 24 h after performance of bacterial instillation or sham operation in $Fpn^{flox/flox}$ and $Fpn^{LysM/LysM}$ mice (n = 6 per group, from 3 independent experiments).

(F) Bacterial burdens in BALF samples were determined 12 h after infection in mice challenged with *E coli* or *K. pneumoniae*. Data are represented as mean ± SEM For comparison between two experimental groups, unpaired two-tailed Student's t-test or nonparametric test was performed. For more than two experimental groups, a one-way ANOVA was performed for comparison. *p< 0.05; **p< 0.01; ****p< 0.0001. FPN = ferroportin; BALF = bronchoalveolar lavage fluid.

function and inflammation, including ultrastructural variance, wet/dry ratios, cell counts and protein exudation (Figure S3). Although LysM is not specific to macrophages, we found that the airway instillation of bone marrow-derived macrophages (BMDMs) from $Fpn^{flox/flox}$ mice significantly aggravated lung injury after *E. coli* infection (Figure S5A), further confirming the contribution of pulmonary macrophage-derived FPN to bacteria-induced lung injury.

Although considering the effect of iron on bacterial growth, we also examined the lung bacterial content and iron levels in mice. As expected, iron levels were lower in BALF and higher in pulmonary macrophages of $Fpn^{LysM/LysM}$ mice than those of $Fpn^{flox/flox}$ mice (Figure S4). Correspondingly, the extracellular bacterial load was significantly reduced in $Fpn^{LysM/LysM}$ mice (Figure 2F). We further constructed another lung injury mouse model by using nonviable (heat-killed) *E. coli*. Of interest, we found that the attenuation of histopathological lung injury was preserved in $Fpn^{LysM/LysM}$ mice (Figure S5B), suggesting that macrophages are involved in the development of lung injury through other potential mechanisms.

FPN deficiency in macrophages benefits pulmonary barrier regeneration during bacteria-induced acute lung injury

To understand the mechanisms underlying the effect of macrophage FPN on the pathogenesis of bacteria-induced acute lung injury, we conducted transcriptomic analysis of lung tissues obtained from $Fpn^{LysM/LysM}$ mice infected with *E. coli* at 12 h or 24 h post infection. Enrichment analysis indicated that barrier regeneration-related processes (*e.g.*, differentiation or proliferation of epithelial or endothelial cells and cell cycle) were significantly enriched in $Fpn^{LysM/LysM}$ mice (Figure 3A). Consistently, the proliferation of respiratory epithelial cells was significantly increased for the beginning of the repair phase in $Fpn^{LysM/LysM}$ mice at 24 h after infection (Figure 3B). Compared with $Fpn^{flox/flox}$ mice after bacterial insult, $Fpn^{LysM/LysM}$ mice exhibited increased expression of α-SMA, which marked the superior infiltration of myofibroblasts for subsequent collagen biosynthesis/deposition (Figures 3C, S6, and S3D). Furthermore, Picrosirius red staining showed that the collagen deposition was increased in lung tissues in infected $Fpn^{LysM/LysM}$ mice, in which a higher proportion of collagen I contributed to high-performance proliferation/regeneration (Figure 3E).

FPN deficiency in macrophages preserves pulmonary barrier integrity by regulating the production of Areg

We next explored the detailed molecular mechanisms of macrophage FPN in pulmonary barrier regeneration. We mapped RNA-seq profiles of pulmonary macrophages isolated from bacteria-challenged mice and identified amphiregulin (Areg), a critical factor in tissue regeneration and barrier protection/repair after lung injury,[9–11] with significantly differential expression (Figure 4A). In parallel, the translational levels of Areg in pulmonary macrophages and BALF from $Fpn^{LysM/LysM}$ mice were markedly increased relative to those in $Fpn^{flox/flox}$ mice after infection (Figures 4B and 4C). Of note, these observations on Areg expression were confirmed in clinical BALF samples collected from ARDS patients with pneumonia (Figure 4D). The contents of Areg in clinical BALF were negatively correlated with the percentage of FPN-positive pulmonary macrophages (Figure 4E). Correspondingly, epidermal growth factor receptor (EGFR), a key receptor of Areg, was significantly activated in *E. coli*-infected $Fpn^{LysM/LysM}$ mice in comparison to that of infected $Fpn^{flox/flox}$ mice (Figure 4F).

To further determine the central role of Areg, we pharmacologically antagonized endogenous Areg by intratracheal administration of an anti-Areg neutralizing antibody. The results demonstrated that $Fpn^{LysM/LysM}$ mice receiving anti-Areg antibody died within 24 h post infection, whereas those receiving IgG showed 50% survival (Figure 4G). After treatment with an anti-Areg antibody after infection, $Fpn^{LysM/LysM}$ mice presented more severe histological lung injury than that of IgG-treated mice (Figure 4H). The administration of anti-Areg antibody also resulted in increased permeability of the alveolar-capillary barrier in infected $Fpn^{LysM/LysM}$ mice (Figure 4I), which was further inferred by the severe damage observed in the pulmonary ultrastructure (Figure S7). In addition, the proliferation of epithelial cells, α-SMA expression, and collagen deposition were worsened by administration of the anti-Areg antibody (Figures 4J–4M).

Iron-induced activation of YAP is involved in the production of Areg in macrophages

To interpret the underlying mechanisms for the regulation of macrophage-derived Areg, we performed a transcription factor prediction analysis based on genomic data of $Fpn^{LysM/LysM}$ pulmonary macrophages after lung injury. This analysis identified three predicted regulator binding sites directly linked to the targeted gene Areg, including Runx, AP1, and Smad (Figure S8); all these sites were related to Yes-associated

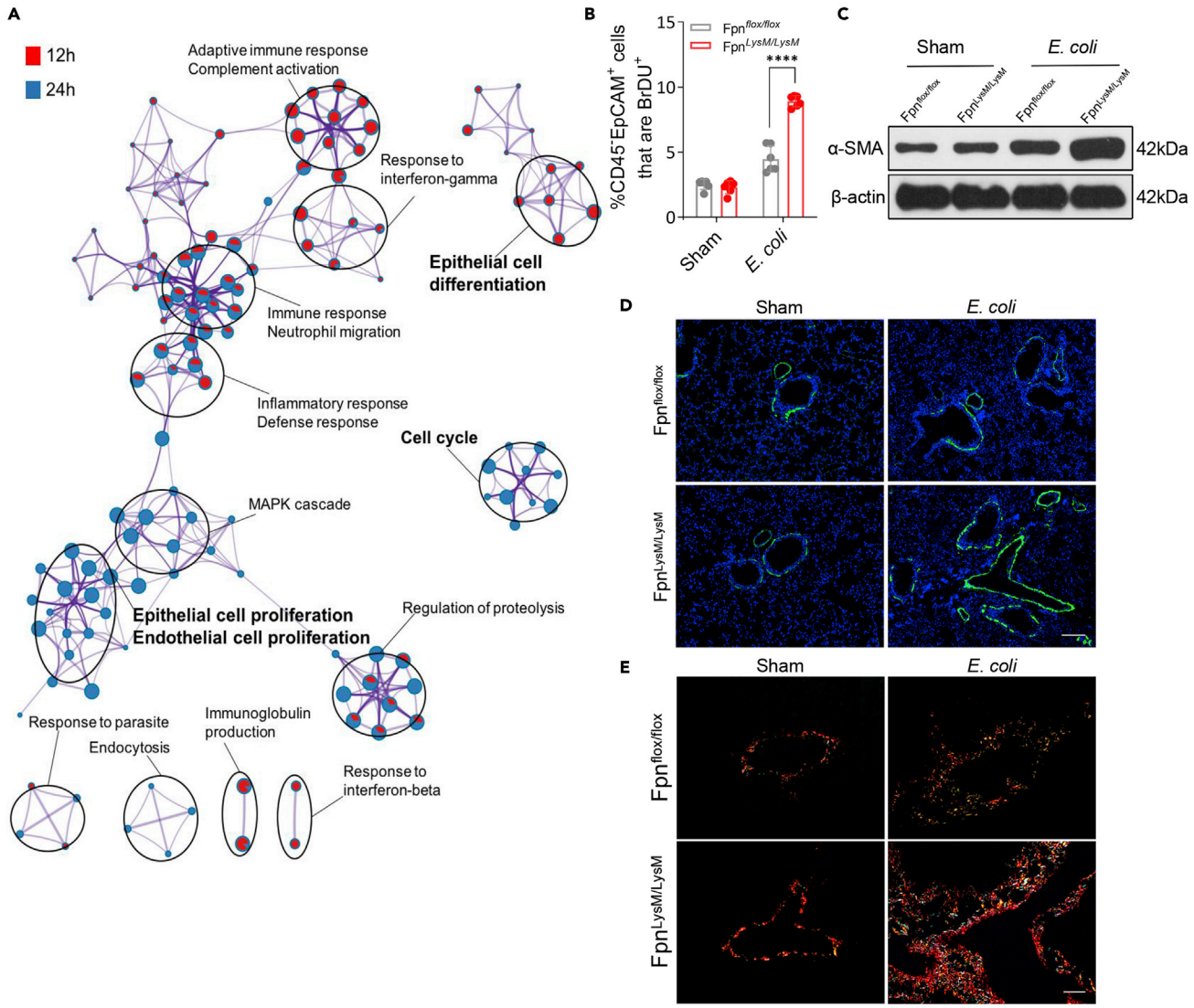

Figure 3. FPN deficiency in macrophages promoted barrier restoration during bacteria-induced acute lung injury

(A) Enrichment network visualization for results at 12 h and 24 h from lung tissues of $Fpn^{flox/flox}$ and $Fpn^{LysM/LysM}$ mice after *E. coli* infection. Nodes are represented by pie charts indicating the proportional number of genes originated from each time point. Color code represents the identities of gene lists.

(B) Percentages of proliferating epithelial cells were measured by flow cytometry after *E. coli* infection.

(C and D) Protein levels of α-SMA by western blot (C) and by immunofluorescence staining (D) in lung at 24 h following *E. coli* infection (n = 6 per group; scale bars, 100μm).

(E) Representative photomicrographs of lung collagen production by Picrosirius Red staining after *E. coli* infection (n = 3 per group; scale bars, 100μm). Type I collagen are shown in red and type III collagen in green. All data are representative of at least two independent experiments (mean ± SEM). For comparison between two experimental groups, unpaired two-tailed Student's t-test or nonparametric test was performed. For more than two experimental groups, a one-way ANOVA was performed for comparison. ****p< 0.0001. FPN = ferroportin; α-SMA = alpha-smooth muscle actin.

protein (YAP), a transcriptional coactivator associated with alveolar epithelium repair and regeneration.[12] Therefore, the activation of YAP (the nonphosphorylated form of YAP with transcriptional activity[13]) was examined and found to be significantly increased after lung injury in pulmonary macrophages and BMDMs from $Fpn^{LysM/LysM}$ mice compared to $Fpn^{flox/flox}$ mice (Figures 5A and 5B). Pharmacological inhibition of YAP by verteporfin dramatically downregulated the protein levels of macrophage-derived Areg (Figures 5C and 5D), suggesting the participation of YAP signaling in the biosynthesis of Areg.

Cellular iron homeostasis was previously found to be dramatically dysregulated in macrophages from $Fpn^{LysM/LysM}$ mice.[14] We then hypothesized that cellular iron might function as a contributing factor for

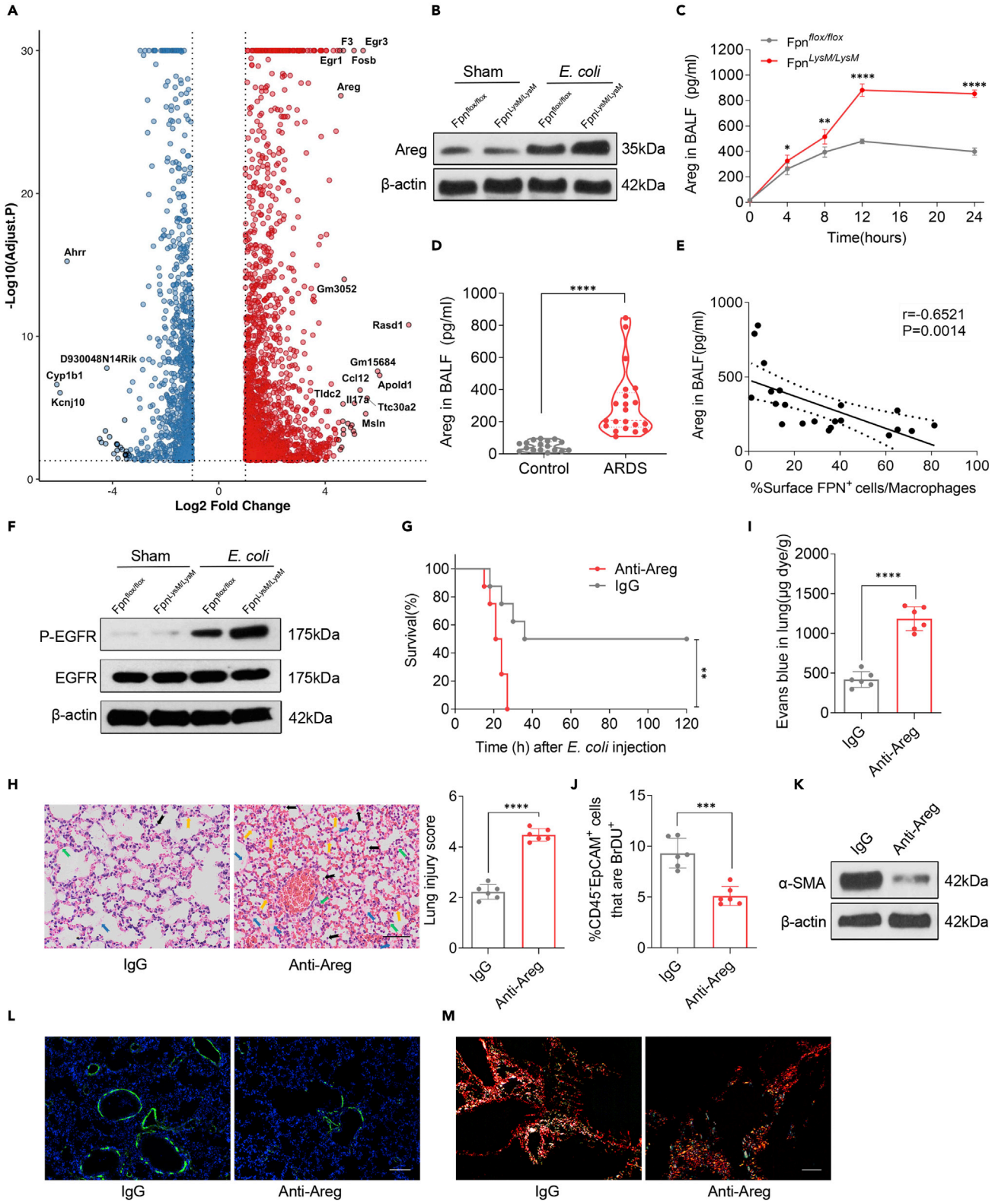
A
-Log10(Adjust.P)
Log2 Fold Change
F3
Egr3
Egr1
Fosb
Areg
Ahrr
Gm3052
Rasd1
D930048N14Rik
Cyp1b1
Kcnj10
Gm15684
Ccl12
Apold1
Tldc2
Il47a
Ttc30a2
Msln
B
Sham
E. coli
Areg
β-actin
35kDa
42kDa
C
Areg in BALF (pg/ml)
Time(hours)
D
Areg in BALF (pg/ml)
Control
ARDS
E
Areg in BALF(pg/ml)
r=-0.6521
P=0.0014
%Surface FPN+ cells/Macrophages
F
P-EGFR
EGFR
β-actin
175kDa
175kDa
42kDa
G
Anti-Areg
IgG
Survival(%)
Time (h) after E. coli injection
I
Evans blue in lung(μg dye/g)
IgG
Anti-Areg
H
IgG
Anti-Areg
Lung injury score
J
%CD45-EpCAM+ cells that are BrDU+
K
α-SMA
β-actin
42kDa
42kDa
L
IgG
Anti-Areg
M
IgG
Anti-Areg

Figure 4. FPN deficiency in macrophages preserved pulmonary barrier integrity via regulating the production of Areg

(A) Volcano plot showing differentially expressed genes in pulmonary macrophages from $Fpn^{flox/flox}$ and $Fpn^{LysM/LysM}$ mice at 12 h affected by *E. coli* infection. Red dots represent overexpressed genes, whereas blue dots represent downregulated genes. The annotated dots are top 25 genes with the most significance.

(B and C) Protein expression of Areg in pulmonary macrophages at 12 h (B) or BALF (C) from $Fpn^{flox/flox}$ and $Fpn^{LysM/LysM}$ mice after *E. coli* infection were evaluated.

(D) Protein levels of Areg in BALF were measured by ELISA in controls (n = 17) and ARDS patients (n = 21).

(E) Correlation of FPN levels with Areg in ARDS patients (n = 21).

(F) Protein levels of P-EGFR and EGFR in lung tissues from $Fpn^{flox/flox}$ and $Fpn^{LysM/LysM}$ mice at 24 h affected by *E. coli* infection. β-actin served as a protein loading control.

(G–M) Mice received treatment with Areg neutralizing antibodies (Anti-Areg, 1 mg/kg) or IgG (1 mg/kg) 30 min after intratracheal challenge with *E. coli*. All samples were taken at 24 h following *E. coli* infection.

(G) Survival of mice after interventions of Anti-Areg or IgG (n = 8 per group).

(H) Representative images of lungs with hematoxylin and eosin staining and quantification of lung injury score (n = 6 per group, from 3 independent experiments; scale bar, 100 μm). Histologic image showing the inflammatory cells infiltration (black arrows), fibrin deposits (blue arrows) and erythrocyte (yellow arrows) in the airspace and alveolar septal thickening (green arrows).

(I) *In vivo* Evans blue dye permeability assay in lungs (n = 6 per group, from 3 independent experiments).

(J) Percentages of proliferating epithelial cells measured by flow cytometry (n = 6 per group).

(K and L) Protein levels of α-SMA by western blot (K) and by immunofluorescence staining (L) in lung (n = 6 per group; scale bars, 100 μm).

(M) Representative photomicrographs of lung collagen production by Picrosirius Red staining (n = 3 per group; scale bars, 100 μm). Type I collagen are shown in red and type III collagen in green. All data are representative of at least two independent experiments (mean ± SEM). For comparison between two experimental groups, unpaired two-tailed Student's t-test or nonparametric test was performed. *p< 0.05; **p< 0.01; ***p< 0.001; ****p< 0.0001. FPN = ferroportin; Areg = amphiregulin; P-EGFR = phospho-epidermal growth factor receptor; α-SMA = alpha-smooth muscle actin.

YAP activity. We found that in BMDMs from $Fpn^{flox/flox}$ mice, the increase in iron content via administration of ferric ammonium citrate significantly facilitated the activation of YAP signaling and promoted the production and secretion of Areg under *E. coli* infection conditions (Figures 5E and 5F). In contrast, reducing iron levels by the iron chelator desferrioxamine (DFO) decreased YAP activity and the protein levels of Areg in BMDMs from both $Fpn^{flox/flox}$ (Figures 5E and 5F) and $Fpn^{LysM/LysM}$ mice (Figures 5G and 5H), further indicating the involvement of FPN in the biosynthesis of Areg via YAP signaling regulated by cellular iron.

The hepcidin-FPN axis mediated the protective effects against bacteria-induced acute lung injury

Hepcidin, a natural degrader of FPN, might be considered a potential therapeutic option for infection. However, hepcidin contains 25 residues with four specifically paired disulfide bridges to stabilize β-sheet conformations; as a result, the synthesis is usually difficult and the process is expensive, thereby limiting clinical translation. Previous efforts predicted the interaction between hepcidin and FPN by using molecular docking simulation and identified minihepcidin, a nonapeptide located in the N-terminus of hepcidin that exhibits an iron-regulating function.[15] Although its structure was significantly simplified, minihepcidin exhibited a significantly weaker activity than that of the parent peptide hepcidin. Thus, we redesigned hepcidin as a simplified peptide with comparable activity. In parallel with previous efforts, molecular dynamics (MD) simulations of the cry-EM structure of the hepcidin-FPN complex identified the crucial pharmacophore of hepcidin that also consists of the N-terminal minihepcidin (Figure 6A). To further improve the activity of minihepcidin, we chemically modified minihepcidin with a cholesteryl group, a hydrophobic block in peptide design,[16,17] onto its N-terminus via a β-Ala linker, producing a lipopeptide with amphiphilic properties. This achieved nanoassembly behavior under weak noncovalent interactions (e.g., van der Waals forces), further enhancing the passive affinity to macrophages and the stability (Figure 6B). All-atomic MD simulation clearly verified that cholesterylation endows the minihepcidin with the self-assembly ability in aqueous solution, forming a core-shell structure (Figure 6C). Thus, supramolecular nanostructures were observed with an average size of 34.12 ± 2.42 nm by using TEM (Figures 6D and S9) and were determined to exhibit no significant cytotoxicity (Figure S10). Hence, cholesteryl minihepcidin was termed C-hepcidin (C-Hep) in the following investigations. Fluorescent assays and flow cytometry showed that C-Hep could effectively bind to FPN in macrophages, similar to native hepcidin (Figure S11). In addition, C-Hep successfully degraded macrophage FPN (Figure 6E and S12), contributing to iron regulation comparable to that of hepcidin (Figure S13).

We then explored the effects of the hepcidin-FPN axis in bacteria-infected murine models by administrating minihepcidin, native hepcidin, and C-Hep. The administration of C-Hep significantly decreased the mortality of lung-injured mice caused by *E. coli* or *K. pneumoniae* compared with those treated with vehicle or minihepcidin (Figures 7A and 7B). Furthermore, C-Hep treatment attenuated lung injury

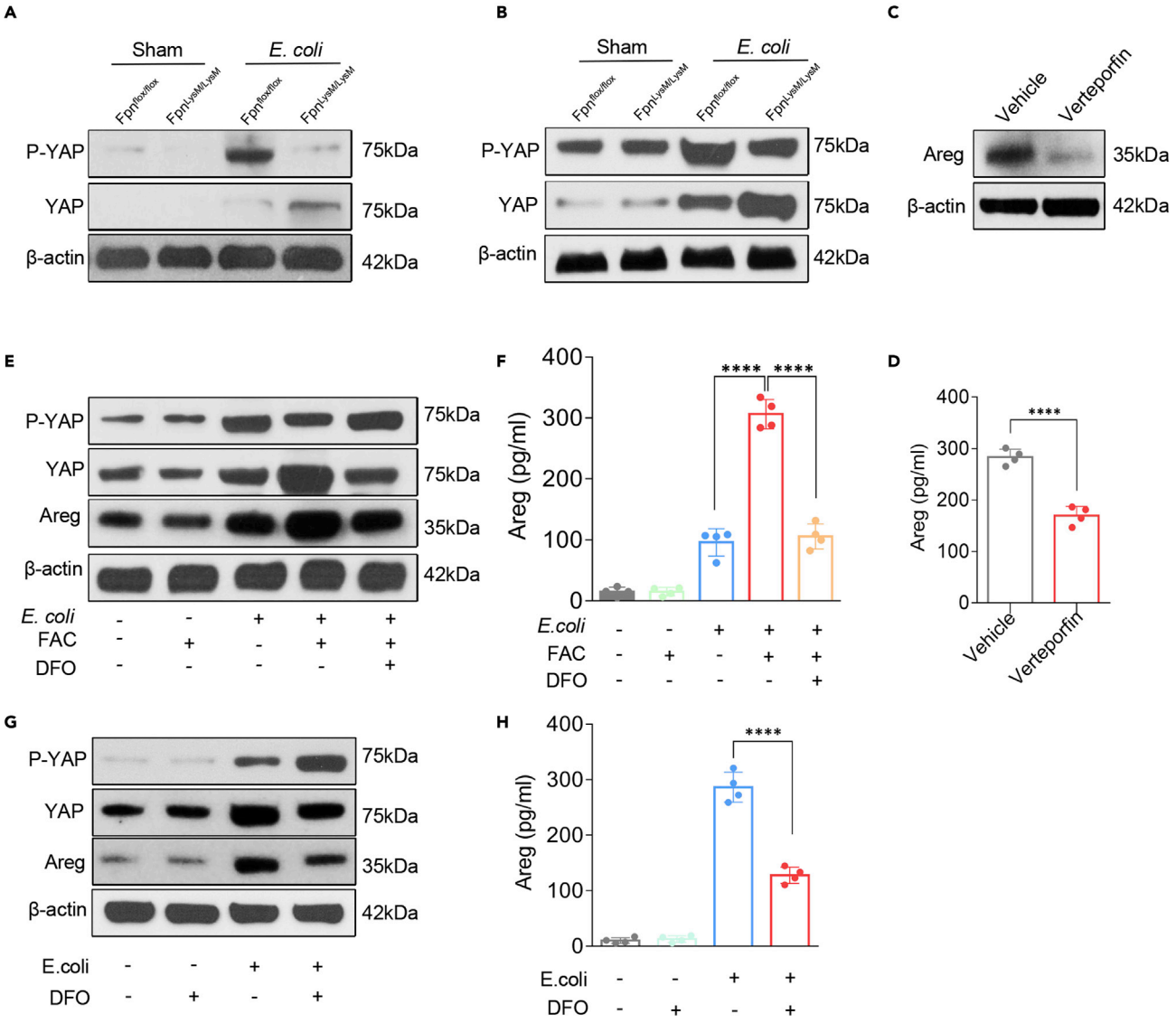

Figure 5. Iron-induced activation of YAP involved in the production of Areg in macrophages

(A and B) Protein levels of P-YAP and YAP in pulmonary macrophages (A) or BMDMs (B) from $Fpn^{flox/flox}$ and $Fpn^{LysM/LysM}$ mice at 12 h affected by *E. coli* infection.

(C and D) Protein expression of Areg in BMDMs (C) or supernatant (D) at 12 h after *E. coli* infection with different interventions (n = 4 per group).

(E and F) Protein levels of P-YAP, YAP and Areg in BMDMs by western blot (E) and Areg in supernatant of BMDMs by ELISA (F) from $Fpn^{flox/flox}$ mice at 12 h affected by *E. coli* infection with different interventions of FAC (100 μM, 20 h) or DFO (100 μM, 12 h) (n = 4 per group).

(G and H) Protein levels of P-YAP, YAP and Areg in BMDMs by western blot (G) and Areg in supernatant by ELISA (H) from $Fpn^{LysM/LysM}$ mice at 12 h affected by *E. coli* infection with intervention of DFO (100 μM, 12 h) (n = 4 per group). All data are representative of at least two independent experiments (mean ± SEM). For comparison between two experimental groups, unpaired two-tailed Student's t-test or nonparametric test was performed. For more than two experimental groups, a one-way ANOVA was performed for comparison. ****p< 0.0001. FPN = ferroportin; Areg = amphiregulin; YAP = yes-associated protein; FAC = ammonium ferric citrate; DFO = Deferoxamine; BMDMs = bone-marrow-derived macrophages.

(Figure 7C) and protected the integrity of the pulmonary barrier (Figure 7D). In addition, the number of epithelial cells, the expression of α-SMA, and collagen deposition were also upregulated after C-Hep therapy (Figures 7E–7H). Consistently, the protein levels of Areg in pulmonary macrophages and BALFs from mice treated with C-Hep were markedly increased (Figures 7I and 7J). Of interest, the protective effect of C-Hep was blocked by anti-Areg neutralizing antibodies (Figure 7K), further confirming the central role of Areg in macrophage FPN-associated lung regeneration. Of note, compared to native hepcidin, the protective effects of C-Hep were comparable in survival rates (Figures 7A and 7B) but more efficient in histological

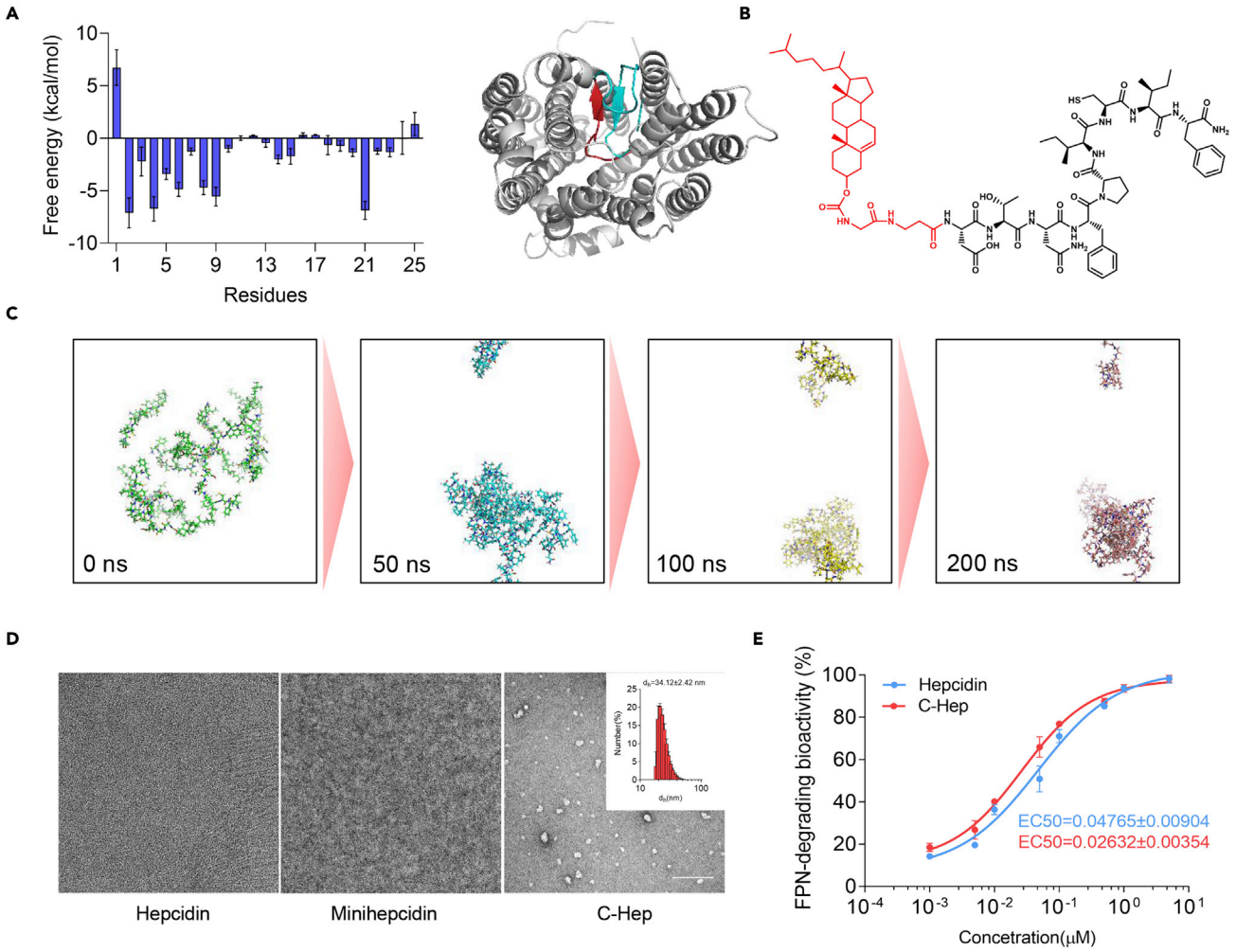

Figure 6. Cholesterylated hepcidin self-assembles into supramolecular nanostructures in solution

(A) Contributions of individual residues in the full-length structure of hepcidin to MM/GBSA binding free energy (left) and pose of hepcidin/Fpn complex after MD simulation (right).

(B) Chemical structure of cholesterolated minihepcidin.

(C) Snapshots of cholesterolated minihepcidin aggregates represent the self-assembly process after 50, 100, and 200 ns production MD simulation.

(D) Transmission electron microscopy (TEM) images of parent hepcidin, minihepcidin and C-hepcidin (C-Hep) in DI water. Scale bars, 100 nm. Inserted pictures show the size distribution of C-Hep determined by dynamic light scattering (DLS).

(E) Quantification of the ferroportin-associated membrane fluorescence in Madin-Darby Canine Kidney cells treated with serial dilutions of either hepcidin or C-Hep for 18 h. The activity was measured by a flow cytometry-based assay detecting the degradation of FPN-GFP (n = 3 per concentration). All data are representative of at least two independent experiments (mean ± SEM). For EC50 values, nonlinear regression [agonist] versus response was performed. ****p< 0.0001. FPN = ferroportin; ns = no significance.

lung injury and pulmonary barrier function (Figures 7C–7J). In addition, no effect on the survival rate was observed in C-Hep-treated $Fpn^{LysM/LysM}$ mice (Figure S14).

DISCUSSION

In the current study, our clinical data revealed that macrophage FPN increased in ARDS patients with bacterial pneumonia and was negatively correlated with the production of Areg and pulmonary oxygenation. We then implemented a clinically relevant, nonsterile acute lung injury model induced by Gram-negative bacteria in mice. We found that FPN deficiency in macrophages significantly reduced lung injury with a decreased mortality rate and improved histological injury. Such protective effects were achieved through preventing extracellular bacterial growth in the lung by limiting extracellular iron availability and regulating Areg to preserve pulmonary barrier function. Iron-induced activation of YAP signaling was involved in the

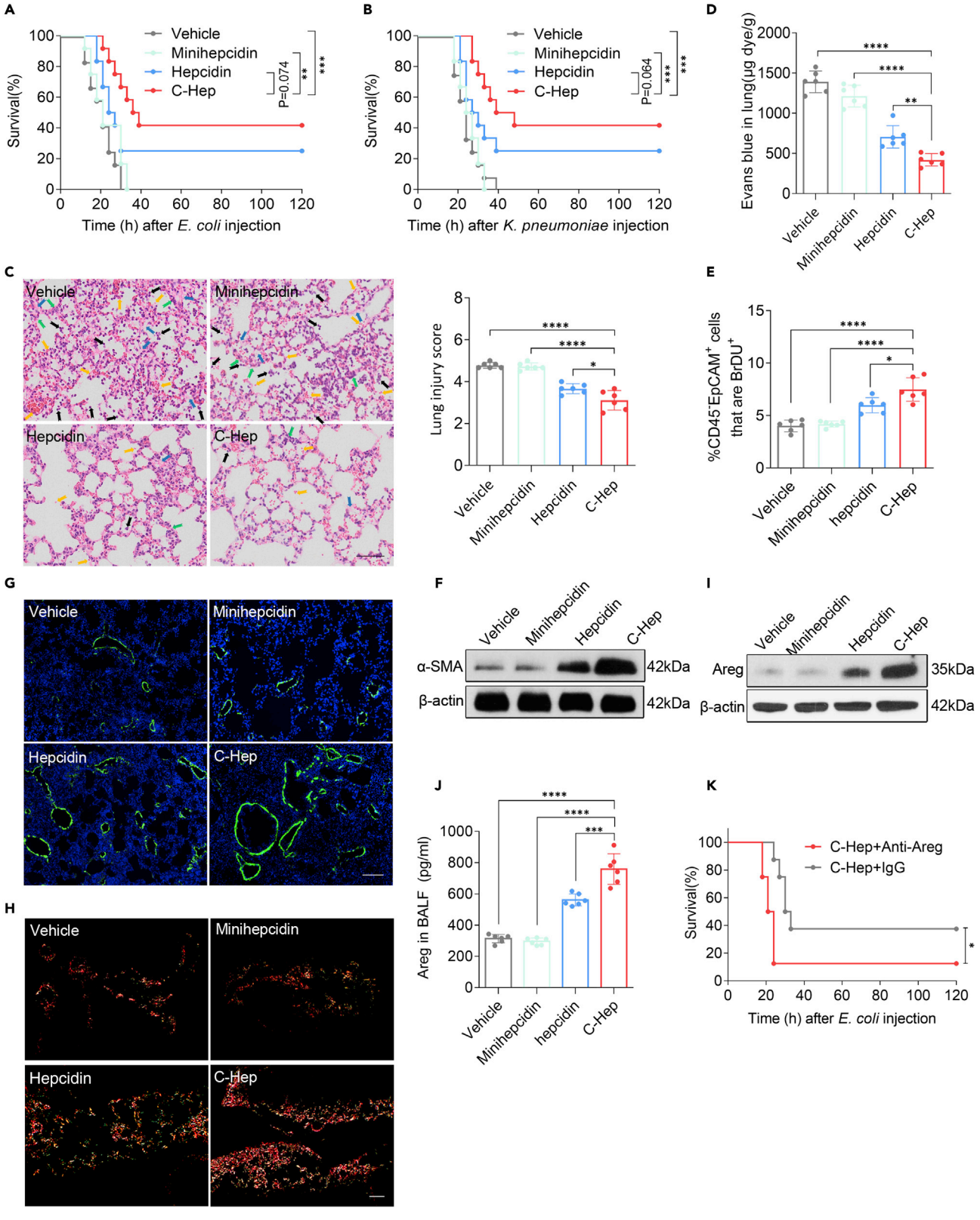
A
Survival(%)
Vehicle
Minihepcidin
Hepcidin
C-Hep
P=0.074
Time (h) after E. coli injection
B
Survival(%)
P=0.064
Time (h) after K. pneumoniae injection
D
Evans blue in lung(μg dye/g)
C
Vehicle
Minihepcidin
Hepcidin
C-Hep
Lung injury score
E
%CD45-EpCAM+ cells that are BrDU+
G
H
F
α-SMA
β-actin
42kDa
I
Areg
35kDa
J
Areg in BALF (pg/ml)
K
C-Hep+Anti-Areg
C-Hep+IgG

Figure 7. The hepcidin-FPN axis mediated the protective effects against bacteria-induced acute lung injury

(A and B) Survival was monitored for mice with different interventions: C-Hep, native hepcidin, minihepcidin or vehicle after infection of *E. coli* (A) or *K. pneumoniae* (B) (n = 12 per group).

(C–K) Mice received treatment with either hepcidin, minihepcidin or C-Hep (25nmols/per mouse) immediately after intratracheal challenge with *E. coli*.

(C) Representative images of lungs with hematoxylin and eosin staining and quantification of lung injury score at 24 h (n = 6 per group; scale bar, 100 μm). Histologic image showing the inflammatory cells infiltration (black arrows), fibrin deposits (blue arrows) and erythrocyte (yellow arrows) in the airspace and alveolar septal thickening (green arrows).

(D) *In vivo* Evans blue dye permeability assay in lungs at 24 h (n = 6 per group).

(E) Percentages of proliferating epithelial cells at 24 h were measured by flow cytometry (n = 6 per group).

(F and G) Protein levels of α-SMA by western blot (F) and by immunofluorescence staining (G) in lung at 24 h (n = 6 per group; scale bars, 100 μm).

(H) Representative photomicrographs of lung collagen production by Picrosirius Red staining at 24 h (n = 3 per group; scale bars, 100 μm). Type I collagen are shown in red and type III collagen in green.(I and J) Protein expression of Areg in pulmonary macrophages (I) or BALF (J) at 12 h.

(K) Survival of mice treated by C-Hep with either Areg neutralizing antibodies or IgG (n = 8 per group). All data are representative of at least two independent experiments (mean ± SEM). For more than two experimental groups, a one-way ANOVA was performed for comparison. *p< 0.05; **p< 0.01; ***p< 0.001; ***p< 0.0001. FPN = ferroportin; Areg = amphiregulin; α-SMA = alpha-smooth muscle actin.

regulation of macrophage-derived Areg. In addition, we documented that the intratracheal administration of C-Hep protected against bacteria-induced lung injury by targeting the FPN pathway. Collectively, these findings uncovered the pathophysiological roles of macrophage FPN in bacteria-induced ARDS and deeply elucidated its underlying mechanisms. Valuably, these findings also suggested the pharmacological therapeutic potential of the hepcidin-FPN axis in treating bacteria-induced ARDS.

ARDS, one of the most life-threatening syndromes in intensive care units, is usually associated with massive inflammatory damage in the alveolar-capillary barrier and subsequent compromised gas exchange.[2] Consequently, therapeutic options capable of diminishing proinflammatory cascades and restoring the alveolar-capillary barrier are urgently needed. Nevertheless, no pharmacological approaches have been successful in specifically treating ARDS through preserving the pulmonary barrier function.

In this study, we initially found a critical and quantitative role of macrophage FPN in respiratory failure. We observed dramatically increased FPN expression in pulmonary macrophages in ARDS patients with bacterial pneumonia, which was negatively correlated with pulmonary oxygenation. We also documented that in myeloid-specific Fpn-deficient mice, the deletion of FPN in pulmonary macrophages contributed to protective effects against bacteria-induced ARDS. It is noteworthy and regrettable that LysM is not specific to macrophages and is also expressed by neutrophils, monocytes, dendritic cells, and type II alveolar epithelial cells. Indeed, the evidence that administration of BMDMs from $Fpn^{flox/flox}$ mice significantly aggravated lung injury after *E. coli* infection could partially confirm the significance of FPN in pulmonary macrophages. In-depth evidence showed that the deficiency of macrophage FPN resulted in the limitation of extracellular bacterial growth in lung. This deficiency in FPN also increased the biosynthesis of Areg through iron-activated YAP signaling, thereby promoting restoration of the pulmonary barrier. Hence, macrophage FPN can be considered a reasonable drug target for therapeutic development to treat ARDS.

In this case, as a natural degrader of FPN, hepcidin can be translated into an ideal therapeutic to treat ARDS by targeting FPN. However, hepcidin presents some inherent shortcomings, such as a difficult process of chemical synthesis, a high cost, and poor pharmacokinetics[18,19]; these disadvantages limit its *in vivo* efficacy and further translational feasibility. Although the introduction of "minihepcidin" significantly simplifies the structure, its activity/stability cannot meet pharmacological acceptability. In particular, in the highly complex infectious microenvironment, bacterial proliferation leads to a significant increase in the expression of pathogenic factors (e.g., phosphatases, phospholipases, proteases, toxins, etc.) in the microenvironment and local acidification.[20] How to restore the activity of minihepcidin to that of its parent compound hepcidin with a simple and stable structure remains a challenge. To resolve this issue, we combined hepcidin with nanomedicine to generate a self-assembled nanoparticle through attaching a cholesteryl moiety (C-hepcidin/C-Hep) at the N-terminal. We found that C-Hep could form a stable supramolecular nanostructure in solution, and compared to minihepcidin and hepcidin, C-Hep exhibited significantly and slightly stronger *in vitro* activity, respectively. More importantly, C-Hep nanoparticles successfully protected mice against bacterial challenge by binding to FPN for its internalized degradation. Of note, the therapeutic efficacy delivered by C-Hep was comparable to that observed with the administration of native hepcidin.

We also found that the therapeutic efficacy of C-Hep was partially attributed to the improvement in lung barrier regeneration. This was verified in the current study by the enhanced proliferation of epithelial cells, differentiation of myofibroblasts and production of collagens after C-Hep treatment. As a natural degrader of FPN with an iron-regulating function, hepcidin or hepcidin analog has been indicated to prevent bacterial dissemination by limiting extracellular iron availability.[4] Other experimental studies also showed its regulation in macrophage function, i.e., phagocytosis and cytokine production, via the degradation of FPN, contributing to its protection in acute lung injury.[5,7,8] However, our findings revealed a previously unrecognized mechanism by which the hepcidin-FPN axis can also direct macrophages to participate in tissue regeneration following injury, thereby preserving pulmonary barrier integrity.

Our findings further revealed that YAP was involved in the hepcidin-FPN axis-mediated tissue regeneration. We identified that the growth factor Areg was significantly increased in macrophages deficient with FPN or treated with C-Hep. Consistent with previous observations of Areg as a transcriptional target of YAP signaling,[21] this finding indicates the activation of YAP in those settings. This was further verified by the increased nonphosphorylated form of YAP in Fpn-knockout pulmonary macrophages and in those with high cellular iron levels. Given that the cellular iron status in macrophages is controlled predominantly by the hepcidin-FPN axis, our finding suggests that YAP may be considered a key downstream molecule for the hepcidin-FPN axis involved in tissue repair. Recently, a mouse study reported that macrophage FPN affected local stromal cell proliferation by regulating iron cycling via a trophic function.[22] Our findings provide the alternative that FPN can direct macrophages toward tissue restoration via Areg production, which results from iron-induced activation of YAP signaling.

In conclusion, the clinical data revealed that the macrophage FPN increased in ARDS patients with bacterial pneumonia and its negative correlation with Areg production and pulmonary oxygenation. Deficiency of FPN in murine macrophages can protect against bacteria-induced lung injury by reducing the extracellular bacterial burden and by preserving pulmonary barrier integrity. Iron-activated YAP signaling is involved in the regulation of macrophage-derived Areg, subsequently contributing to tissue restoration. By degradation of FPN in macrophages, therapeutic treatment with C-Hep attenuates lung injury induced by pneumonia. Together, the results indicate that the modulation of hepcidin-FPN axis in macrophages represents a fascinating and pathophysiological sound approach for the treatment of acute lung injury, promising future clinical translation.

Limitations of the study

We explored the role of macrophage FPN in acute lung injury using $Fpn^{LysM/LysM}$ mice. Although FPN is mainly expressed in placental syncytiotrophoblast cells, duodenal mature enterocytes, reticuloendothelial macrophages and hepatocytes, it is also expressed to a lesser extent in neutrophils and type II alveolar epithelial cells. It is noteworthy and regrettable that LysM is not specific to macrophages and is also expressed by other myeloid lineage cells (neutrophils, all dendritic cell subsets, and monocyte-lineage cells) as well as type II alveolar epithelial cells. Some more specific methods (e.g., $Fpn^{F4/80/F4/80}$ mice) will be employed to explore the physiological role of macrophage FPN in a future study.

STAR★METHODS

Detailed methods are provided in the online version of this paper and include the following:

- KEY RESOURCES TABLE
- RESOURCE AVAILABILITY
  - Lead contact
  - Materials availability
  - Data and code availability
- EXPERIMENTAL MODEL AND SUBJECT DETAILS
  - Human subjects
  - Animals
  - Acute lung injury mouse model
- METHOD DETAILS
  - Peptide/peptidomimetic synthesis
  - Transmission electron microscopy (TEM)
  - Dynamic light scattering (DLS)

- RNA sequencing and analysis
- Molecular dynamics (MD) simulations
- Histopathological analysis
- *In vivo* lung permeability assay
- Immunofluorescence staining
- Lung epithelial proliferation assay
- Murine macrophage isolation and culture
- Western blot
- Iron determination
- Statistical analysis

SUPPLEMENTAL INFORMATION

Supplemental information can be found online at https://doi.org/10.1016/j.isci.2022.105698.

ACKNOWLEDGMENTS

We are grateful to those patients for donating their BALF for the study. We thank Prof. Qiang Shu and Prof. Qixing Chen in the National Clinical Research Center for Child Health, Children's Hospital, School of Medicine, Zhejiang University, for help with discussion of the manuscript; Ms. Chenyu Yang and Yuchen Zhang in the Center of Cryo-Electron Microscopy (CCEM), Zhejiang University, for their excellent technical assistance on TEM imaging; Prof. Wuyuan Lu in the Key Laboratory of Medical Molecular Virology (MOE/NHC/CAMS), School of Basic Medical Sciences, Fudan University, for his professionally technical support on molecular dynamic simulation. This study was supported by the National Natural Science Foundation of China (81720108025 and 81701947).

AUTHOR CONTRIBUTIONS

Conceptualization, H.W., C.Z., and and X.F.; Methodology, H.W., C.Z., and G.L.; Investigation, H.W., G.L., Y.S., J.Z., Y.G., H.Y., J.M., S.C., Y.Z., and K.Z.; Writing – Original Draft, H.W., C.Z., and G.L.; Writing – Review and Editing, M.V.M. and X.F.; Funding Acquisition, X.F. and C.Z.; Resources, X.F., Z.X., C.Z., G.L., and H.W.; Visualization, J.Z., G.L., and H.W.; Supervision, Y.Z., J.Z., and Y.G.

DECLARATION OF INTERESTS

The authors declare that they have no competing interests.

INCLUSION AND DIVERSITY

We support inclusive, diverse, and equitable conduct of research.

Received: February 9, 2022
Revised: July 10, 2022
Accepted: November 25, 2022
Published: December 22, 2022

REFERENCES

1. Matthay, M.A., Ware, L.B., and Zimmerman, G.A. (2012). The acute respiratory distress syndrome. J. Clin. Invest. *122*, 2731–2740.

2. Ware, L.B., and Matthay, M.A. (2000). The acute respiratory distress syndrome. N. Engl. J. Med. *342*, 1334–1349.

3. Rubenfeld, G.D., Caldwell, E., Peabody, E., Weaver, J., Martin, D.P., Neff, M., Stern, E.J., and Hudson, L.D. (2005). Incidence and outcomes of acute lung injury. N. Engl. J. Med. *353*, 1685–1693.

4. Michels, K.R., Zhang, Z., Bettina, A.M., Cagnina, R.E., Stefanova, D., Burdick, M.D., Vaulont, S., Nemeth, E., Ganz, T., and Mehrad, B. (2017). Hepcidin-mediated iron sequestration protects against bacterial dissemination during pneumonia. JCI Insight *2*, e92002.

5. Zeng, C., Chen, Q., Zhang, K., Chen, Q., Song, S., and Fang, X. (2015). Hepatic hepcidin protects against polymicrobial sepsis in mice by regulating host iron status. Anesthesiology *122*, 374–386.

6. Frazier, M.D., Mamo, L.B., Ghio, A.J., and Turi, J.L. (2011). Hepcidin expression in human airway epithelial cells is regulated by interferon-γ. Respir. Res. *12*, 100.

7. Chen, Q.X., Song, S.W., Chen, Q.H., Zeng, C.L., Zheng, X., Wang, J.L., and Fang, X.M. (2014). Silencing airway epithelial cell-derived hepcidin exacerbates sepsis induced acute lung injury. Crit. Care *18*, 470.

8. Yang, Y., Zeng, C., Yang, S., Zhang, Y., Song, S., Liu, S., Shu, Q., Fang, X., and Chen, Q. (2020). Airway epithelial hepcidin coordinates lung macrophages and immunity against bacterial pneumonia. Shock *54*, 402–412.

9. Arpaia, N., Green, J.A., Moltedo, B., Arvey, A., Hemmers, S., Yuan, S., Treuting, P.M., and Rudensky, A.Y. (2015). A distinct function of regulatory T cells in tissue protection. Cell *162*, 1078–1089.

10. Jamieson, A.M., Pasman, L., Yu, S., Gamradt, P., Homer, R.J., Decker, T., and Medzhitov, R. (2013). Role of tissue protection in lethal respiratory viral-bacterial coinfection. Science *340*, 1230–1234.

11. Monticelli, L.A., Sonnenberg, G.F., Abt, M.C., Alenghat, T., Ziegler, C.G.K., Doering, T.A., Angelosanto, J.M., Laidlaw, B.J., Yang, C.Y., Sathaliyawala, T., et al. (2011). Innate lymphoid cells promote lung-tissue homeostasis after infection with influenza virus. Nat. Immunol. *12*, 1045–1054.

12. LaCanna, R., Liccardo, D., Zhang, P., Tragesser, L., Wang, Y., Cao, T., Chapman, H.A., Morrisey, E.E., Shen, H., Koch, W.J., et al. (2019). Yap/Taz regulate alveolar regeneration and resolution of lung inflammation. J. Clin. Invest. *129*, 2107–2122.

13. Dey, A., Varelas, X., and Guan, K.L. (2020). Targeting the Hippo pathway in cancer, fibrosis, wound healing and regenerative medicine. Nat. Rev. Drug Discov. *19*, 480–494.

14. Zhang, Z., Zhang, F., An, P., Guo, X., Shen, Y., Tao, Y., Wu, Q., Zhang, Y., Yu, Y., Ning, B., et al. (2011). Ferroportin1 deficiency in mouse macrophages impairs iron homeostasis and inflammatory responses. Blood *118*, 1912–1922.

15. Preza, G.C., Ruchala, P., Pinon, R., Ramos, E., Qiao, B., Peralta, M.A., Sharma, S., Waring, A., Ganz, T., and Nemeth, E. (2011). Minihepcidins are rationally designed small peptides that mimic hepcidin activity in mice and may be useful for the treatment of iron overload. J. Clin. Invest. *121*, 4880–4888.

16. Xia, S., Liu, M., Wang, C., Xu, W., Lan, Q., Feng, S., Qi, F., Bao, L., Du, L., Liu, S., et al. (2020). Inhibition of SARS-CoV-2 (previously 2019-nCoV) infection by a highly potent pan-coronavirus fusion inhibitor targeting its spike protein that harbors a high capacity to mediate membrane fusion. Cell Res. *30*, 343–355.

17. de Vries, R.D., Schmitz, K.S., Bovier, F.T., Predella, C., Khao, J., Noack, D., Haagmans, B.L., Herfst, S., Stearns, K.N., Drew-Bear, J., et al. (2021). Intranasal fusion inhibitory lipopeptide prevents direct-contact SARS-CoV-2 transmission in ferrets. Science *371*, 1379–1382.

18. Jordan, J.B., Poppe, L., Haniu, M., Arvedson, T., Syed, R., Li, V., Kohno, H., Kim, H., Schnier, P.D., Harvey, T.S., et al. (2009). Hepcidin revisited, disulfide connectivity, dynamics, and structure. J. Biol. Chem. *284*, 24155–24167.

19. Schmidt, P.J., and Fleming, M.D. (2014). Modulation of hepcidin as therapy for primary and secondary iron overload disorders: preclinical models and approaches. Hematol. Oncol. Clin. N. Am. *28*, 387–401.

20. Wang, Z., Liu, X., Duan, Y., and Huang, Y. (2022). Infection microenvironment-related antibacterial nanotherapeutic strategies. Biomaterials *280*, 121249.

21. Zhang, J., Ji, J.Y., Yu, M., Overholtzer, M., Smolen, G.A., Wang, R., Brugge, J.S., Dyson, N.J., and Haber, D.A. (2009). YAP-dependent induction of amphiregulin identifies a non-cell-autonomous component of the Hippo pathway. Nat. Cell Biol. *11*, 1444–1450.

22. Recalcati, S., Gammella, E., Buratti, P., Doni, A., Anselmo, A., Locati, M., and Cairo, G. (2019). Macrophage ferroportin is essential for stromal cell proliferation in wound healing. Haematologica *104*, 47–58.

23. Meyer, K.C., Raghu, G., Baughman, R.P., Brown, K.K., Costabel, U., du Bois, R.M., Drent, M., Haslam, P.L., Kim, D.S., Nagai, S., et al. (2012). An official American Thoracic Society clinical practice guideline: the clinical utility of bronchoalveolar lavage cellular analysis in interstitial lung disease. Am. J. Respir. Crit. Care Med. *185*, 1004–1014.

24. Bharat, A., Bhorade, S.M., Morales-Nebreda, L., McQuattie-Pimentel, A.C., Soberanes, S., Ridge, K., DeCamp, M.M., Mestan, K.K., Perlman, H., Budinger, G.R.S., and Misharin, A.V. (2016). Flow cytometry reveals similarities between lung macrophages in humans and mice. Am. J. Respir. Cell Mol. Biol. *54*, 147–149.

25. Wang, B., Wang, M., Zhang, W., Xiao, T., Chen, C.H., Wu, A., Wu, F., Traugh, N., Wang, X., Li, Z., et al. (2019). Integrative analysis of pooled CRISPR genetic screens using MAGeCKFlute. Nat. Protoc. *14*, 756–780.

26. Zhou, Y., Zhou, B., Pache, L., Chang, M., Khodabakhshi, A.H., Tanaseichuk, O., Benner, C., and Chanda, S.K. (2019). Metascape provides a biologist-oriented resource for the analysis of systems-level datasets. Nat. Commun. *10*, 1523.

27. Janky, R., Verfaillie, A., Imrichová, H., Van de Sande, B., Standaert, L., Christiaens, V., Hulselmans, G., Herten, K., Naval Sanchez, M., Potier, D., et al. (2014). iRegulon: from a gene list to a gene regulatory network using large motif and track collections. PLoS Comput. Biol. *10*, e1003731.

28. Tian, C., Kasavajhala, K., Belfon, K.A.A., Raguette, L., Huang, H., Migues, A.N., Bickel, J., Wang, Y., Pincay, J., Wu, Q., and Simmerling, C. (2020). ff19SB: amino-acid-specific protein backbone parameters trained against quantum mechanics energy surfaces in solution. J. Chem. Theor. Comput. *16*, 528–552.

29. Wang, J., Wolf, R.M., Caldwell, J.W., Kollman, P.A., and Case, D.A. (2004). Development and testing of a general amber force field. J. Comput. Chem. *25*, 1157–1174.

30. Sun, H., Li, Y., Tian, S., Xu, L., and Hou, T. (2014). Assessing the performance of MM/PBSA and MM/GBSA methods. 4. Accuracies of MM/PBSA and MM/GBSA methodologies evaluated by various simulation protocols using PDBbind data set. Phys. Chem. Chem. Phys. *16*, 16719–16729.

31. Jakalian, A., Jack, D.B., and Bayly, C.I. (2002). Fast, efficient generation of high-quality atomic charges. AM1-BCC model: II. Parameterization and validation. J. Comput. Chem. *23*, 1623–1641.

32. Pettersen, E.F., Goddard, T.D., Huang, C.C., Couch, G.S., Greenblatt, D.M., Meng, E.C., and Ferrin, T.E. (2004). UCSF Chimera–a visualization system for exploratory research and analysis. J. Comput. Chem. *25*, 1605–1612.

33. Bragonzi, A., Paroni, M., Nonis, A., Cramer, N., Montanari, S., Rejman, J., Di Serio, C., Döring, G., and Tümmler, B. (2009). Pseudomonas aeruginosa microevolution during cystic fibrosis lung infection establishes clones with adapted virulence. Am. J. Respir. Crit. Care Med. *180*, 138–145.

34. Lai, D., Tang, J., Chen, L., Fan, E.K., Scott, M.J., Li, Y., Billiar, T.R., Wilson, M.A., Fang, X., Shu, Q., and Fan, J. (2018). Group 2 innate lymphoid cells protect lung endothelial cells from pyroptosis in sepsis. Cell Death Dis. *9*, 369.

35. Radu, M., and Chernoff, J. (2013). An in vivo assay to test blood vessel permeability. JoVEe50062.

36. Chapman, H.A., Li, X., Alexander, J.P., Brumwell, A., Lorizio, W., Tan, K., Sonnenberg, A., Wei, Y., and Vu, T.H. (2011). Integrin α6β4 identifies an adult distal lung epithelial population with regenerative potential in mice. J. Clin. Invest. *121*, 2855–2862.

37. Chen, Q., Zhang, K., Jin, Y., Zhu, T., Cheng, B., Shu, Q., and Fang, X. (2013). Triggering receptor expressed on myeloid cells-2 protects against polymicrobial sepsis by enhancing bacterial clearance. Am. J. Respir. Crit. Care Med. *188*, 201–212.

STAR★METHODS

KEY RESOURCES TABLE

REAGENT or RESOURCE	SOURCE	IDENTIFIER
Antibodies		
Human BD Fc Block™	BD Pharmingen	cat#564219;RRID:AB_2728082
FITC Mouse Anti-Human CD45	BD Pharmingen	cat#555482; RRID:AB_395874
eBioscience™ Fixable Viability Dye eFluor™ 455UV	ThermoFisher	cat#65-0868-14
BV510 Mouse Anti-Human CD11b	BD Pharmingen	cat#563088; RRID:AB_2737996
Alexa Fluor®700 Mouse Anti-Human HLA-DR	BD Pharmingen	cat#560743; RRID:AB_1727526
PerCP-Cy™5.5 Mouse Anti-Human CD15	BD Pharmingen	cat#560828; RRID:AB_10563612
Human Ferroportin/SLC40A1 Antibody	R&D	cat#MAB9924
Donkey anti-Rabbit IgG (H+L) Highly Cross-Adsorbed Secondary Antibody, Alexa Fluor™ 594	ThermoFisher	cat#A-21207; RRID:AB_141637
Normal Goat IgG Control	R&D	cat#AB-108-C
Mouse Amphiregulin Antibody	R&D	cat#AF989
anti-alpha smooth muscle Actin antibody	abcam	cat#ab7817
goat anti-rabbit IgG, Alexa Fluor 488	ThermoFisher	cat#A-10680
anti-CD45 antibody	eBioscience	cat#56-0451-82; RRID:AB_891454
anti-mouse CD326 (Ep-CAM) Antibody	biolegend	cat#118207; RRID:AB_1134106
anti-BrdU Antibody	biolegend	cat#339812; RRID:AB_1626188
anti-mouse ferroportin antibody	Alpha Diagnostic International	cat#MTP11-A
anti-alpha smooth muscle Actin antibody	Huabio	cat#ET1607-43
anti-Areg antibody	absin	cat#abs115815
anti-EGFR antibody	abcam	cat#ab52894
anti-EGFR (phospho Y1068) antibody [EP774Y]	abcam	cat#ab40815
anti-YAP antibody	Cell Signaling Technology	cat#14074
anti-Phospho-YAP antibody	Cell Signaling Technology	cat#13008
anti-β-Actin antibody	sigma	cat#A5441
Goat anti-Rabbit IgG (H+L) HRP Conjugated	MultiSciences	cat#GAR0072
goat anti-Mouse IgG (H+L) HRP Conjugated	MultiSciences	cat#GAM0072
Bacterial and virus strains		
Escherichia coli	ATCC	ATCC: 25922
Klebsiella pneumoniae	ATCC	ATCC: 13883
Chemicals, peptides, and recombinant proteins		
Hepcidin	Chinese Peptide	N/A
Minihepcidin	Chinese Peptide	N/A
C-Hep	Chinese Peptide	N/A
RIPA Buffer	Applygen	Cat#C1053
4% Paraformaldehyde Solution	biosharp	Cat# BL539A
SAKURA Tissue-Tek® O.C.T	SAKURA	Cat# 4583
Tween-20	Sigma-Aldrich	Cat# P7949-500ML

(*Continued on next page*)

Continued

REAGENT or RESOURCE	SOURCE	IDENTIFIER
Bovine Serum Albumin	Sigma-Aldrich	Cat# A2153-100G
Certified Fetal Bovine Serum	Biological Industries	Cat# 04-001-1ACS
Triton X-100	Sigma-Aldrich	Cat# X100-500ML
DAPI-Fluoromount-G	SouthernBiotech	Cat# 0100-20
TRIzol™ Reagent	Ambion	Cat#15596018
Red Blood Cell Lysing Buffer	Sigma-Aldrich	Cat#R7757
Recombinant Murine GM-CSF	peprotech	Cat#315-03
DMEM, high glucose, pyruvate	Gibco	Cat#11995065
RPMI 1640 Medium	Biological Industries	Cat#01-100-1A
0.25% Trypsin-EDTA	BasalMedia	Cat#S310JV
Antibiotic Antimycotic Solution (100×), Stabilized	Sigma-Aldrich	Cat#A5955
Evans Blue Dye	Sigma-Aldrich	Cat#E2129
Formamide	Sigma-Aldrich	Cat#F9037
Liberase TM	Roche	Cat#5401127001
BrdU (5-bromo-2′-deoxyuridine), Thymidine analog	Abcam	Cat#ab142567
Pierce™ BCA Protein Assay Kit	ThermoFisher	Cat#23225
Critical commercial assays		
EZ-ECL Kit	Biological Industries	Cat#20-500-120
Mouse TNF-α ValukineTM ELISA	Novus	Cat#VAL609
Mouse IL-1 beta Valukine ELISA Kit	Novus	Cat#VAL601
Experimental models: Cell lines		
Madin-Darby Canine Kidney cells	ATCC	CCL-34
L929 cell line	ATCC	CCL-1
MLE12	ATCC	CRL-2110
Experimental models: Organisms/strains		
Mouse:Fpn$^{LysM/LysM}$	Zhang et al., 2011	N/A
Mouse:Fpn$^{flox/flox}$	Zhang et al., 2011	N/A
Mouse: C57BL/6 wild-type (WT)	Sippr-BK Laboratory Animal Corporation	N/A
Software and algorithms		
FlowJo	TreeStar FlowJo LLC	https://www.flowjo.com/
GraphPad Prism	GraphPad Software	https://www.graphpad.com
ImageJ	NIH	https://imagej.nih.gov/ij/
R statistical package edgeR	Empirical analysis of Digital Gene Expression in R	http://www.bioconductor.org/packages/release/bioc/html/edgeR.html/
Amber 20	Amber	https://ambermd.org/
pymol	schrodinger	https://pymol.org/2/
Other		
RNA-Seq data	NCBI	PRJNA857344

RESOURCE AVAILABILITY

Lead contact

Further information and requests for resources and reagents should be directed to and will be fulfilled by the lead contact, Xiangming Fang (xmfang@zju.edu.cn).

Materials availability

This study did not generate new unique reagents.

Data and code availability

- The RNA-Seq data reported in this paper have been deposited in the National Center for Biotechnology Information Sequence Read Archive. https://www.ncbi.nlm.nih.gov/sra/?term=PRJNA857344.
- This paper does not report original code.
- Any additional information required to reanalyze the data reported in this paper is available from the lead contact upon request.

EXPERIMENTAL MODEL AND SUBJECT DETAILS

Human subjects

All studies were approved by the Clinical Research Ethics Committee of the First Affiliated Hospital of Zhejiang University School of Medicine (IIT20200347A-R1). Patient samples were obtained from discarded excess samples from clinically indicated bronchoscopies under a waiver of consent. Informed consent was obtained from all subjects or their surrogates. Bronchoscopy with bronchoalveolar lavage (BAL) is performed for diagnosis or treatment if ARDS patients due to bacterial pneumonia meet the following criteria: (a) 2012 Berlin Definition for ARDS; (b) radiographic abnormalities; (c) 1 or more of the following clinical signs: fever, purulent endotracheal secretions, or leukocytosis; and (d) no new antimicrobial drugs for 72 h. The control group included ICU patients that needed mechanical ventilation support who were unconscious after craniocerebral trauma surgery. The control group with poor coughing ability received fiberoptic bronchoscopy to clear secretions and lavage to determine the presence of infection. Samples were excluded if (a) the sample was procured from a subject with burns, prior solid organ/stem cell transplant, active malignancy, or human immunodeficiency virus and (b) there was microbiologic evidence of pulmonary infection in control subjects.

Bronchoscopy was performed using a flexible video-bronchoscope following mild sedation and local anesthesia with 2% lidocaine. BAL was performed by instillation of sterile saline (10–20 mL each time for a total of 60-120 mL).[23] Sample processing for flow cytometric analysis and panel design were performed as follows.[24] Briefly, single-cell suspensions were prepared and incubated with Human BD Fc Block (clone Fc1.3216, BD Pharmingen, 564,219) for 20 min on ice to block Fc receptors before staining. The following antibodies were used in the experiments: FITC Mouse Anti-Human CD45 (BD Pharmingen, 555482), eBioscience™ Fixable Viability Dye eFluor™ 455UV (ThermoFisher, 65-0868-14), BV510 Mouse Anti-Human CD11b (BD Pharmingen, 563088), Alexa Fluor® 700 Mouse Anti-Human HLA-DR (BD Pharmingen, 560743), PerCP-Cy™5.5 Mouse anti-human CD15 (BD Pharmingen, 560828), human ferroportin/SLC40A1 antibody (R&D, MAB9924) and Alexa Fluor 594-labeled donkey anti-rabbit secondary antibody (ThermoFisher, A-21207) were used. Details of the immunostaining and gating strategies are described in Figure S15.

Animals

C57BL/6 wild-type (WT) mice aged 6–8 weeks were purchased from Sippr-BK Laboratory Animal Corporation (Shanghai, China). Mice with myeloid lineage-specific ferroportin deletion ($Fpn^{LysM/LysM}$) on a 129/SvEvTac genetic background were a gift from Dr. Fudi Wang (Zhejiang University, Hangzhou, China).[14] $Fpn^{LysM/LysM}$ mice and their littermate controls ($Fpn^{flox/flox}$) were housed under standard care conditions. All animal studies were conducted using male mice and approved by the Animal Care and Use Committee of Zhejiang University (Hangzhou, China), and the animals were handled in accordance with the National Institutes of Health guidelines for ethical animal treatment.

Acute lung injury mouse model

Bacteria-induced acute lung injury mouse models were induced by intratracheal instillations of varying amounts of bacteria.[8,33] In detail, 50 μL of PBS containing 2.5×10^6 colony-forming units (CFU) of *Escherichia coli* (*E. coli*, ATCC 25922) or 5×10^7 CFU of *Klebsiella pneumoniae* (*K. pneumoniae*, ATCC 13883) was intratracheally administered to mice. To further explore the role of Areg in $Fpn^{LysM/LysM}$ mice during lung injury, mice were treated intratracheally with IgG (normal goat IgG control, R&D, AB-108-C, 25 μg/mouse) or anti-Areg antibodies (mouse amphiregulin antibody, R&D, AF989, 25 μg/mouse) 30 min after pulmonary

bacterial infections. To assess the therapeutic effects of native hepcidin or C-Hep against bacteria-induced acute lung injury, hepcidin (20 nmoles/mouse), minihepcidin (20 nmoles/mouse), C-Hep (20 nmoles/mouse) or an equal volume of vehicle (1.25% DMSO +98.75% ddH_2O, 50 μL) was administered to mice intratracheally after pulmonary bacterial infections. Mortality was assessed hourly.

METHOD DETAILS

Peptide/peptidomimetic synthesis

All peptides or peptidomimetic compounds in this study were synthesized using solid phase peptide synthesis (SPPS) by Chinese Peptide (Hangzhou, China). The molecular weight and purity of each compound were verified by ESI-MS and RP-HPLC, respectively (Figures S16–S18).

Transmission electron microscopy (TEM)

To characterize the supramolecular nanostructure of C-Hep, its solution with a concentration of 100 μg/mL was dropped onto a 300-mesh copper grid coated with carbon. A few minutes after deposition, the residual solvent was removed using filter papers, and then the samples were dried at room temperature. Negative staining was performed using a 2 wt. % aqueous uranyl acetate solution. After that, the ultrastructure of C-Hep was observed under a Tecnai G2 Spirit 120 kV transmission electron microscope (Thermo FEI, USA).

Dynamic light scattering (DLS)

To reveal the average particle size, the hydrodynamic diameters (d_h) and number distribution of ND (100 μg/mL) were monitored by the DLS principle using a Malvern Nano-ZS90 instrument (Malvern, UK).

RNA sequencing and analysis

Lung tissues or isolated pulmonary macrophages from mice with bacterial infection were subjected to parallel RNA sequencing using the Illumina HiSeq platform (Novogene Experimental Department). Gene expression was quantified using the fragments per kilobase of exon per million mapped reads method and were analyzed for differential expression by the R statistical package edgeR (Empirical analysis of Digital Gene Expression in R, http://www.bioconductor.org/packages/release/bioc/html/edgeR.html/). The differentially expressed genes were defined by an absolute fold change >2 and a false discovery rate <0.05 and visualized by volcano plot using the R package MAGeCKFlute.[25] To link differentially expressed genes to known biological functions, gene ontology analysis was performed by using a web-based portal Metascape.[26] The enrichment network was also visualized in Metascape for gene ontology results at 12 h and 24 h from lung tissues of $Fpn^{flox/flox}$ and $Fpn^{LysM/LysM}$ mice after *E. coli* infection. To predict potential transcription regulators involved in the observed gene expression patterns, transcription factor prediction analysis was performed in iRegulon (version 1.3) in combination with the provided 10K position weight matrix motif collection.[27]

Molecular dynamics (MD) simulations

The cryo-EM structure of the hepcidin/FPN complex (PDB ID: 6WBV) was selected as the initial coordinate to analyze the detailed interactions between hepcidin and FPN through all-atomic MD simulation. Before MD simulation, the molecular mechanics parameters from the ff19SB fore field, GAFF force field, and *water.tip3p* force field were assigned to the hepcidin/FPN complex, which was subsequently neutralized by adding sodium/chlorine counter ions and solvated in a cuboid box of transferable interatomic potential with three points model (TIP3P) water molecules with solvent layers 12.0 Å between solute surface and box edges, by using the LEaP module of Amber 20.[28,29] The SHAKE algorithm was employed to restrict all covalent bonds involving hydrogen atoms. The *pmemd. MPI* module was used to perform the minimization, heat, density and equilibration of the solvated hepcidin/FPN system. Initially, two steps of minimization were performed, containing which involved a 10000-cycle minimization with main chain restrained and a 10000-cycle nonrestrained minimization, thereby removing unfavorable contacts. The system was then heated from 0 K to 300 K in 40 ps and maintained at 300 K for 10 ps using Langevin dynamics at a constant volume with a time step of 1 fs. Then, 50 ps of density equilibration was applied to the system, which subsequently underwent two steps of NPT (T = 300 K, p = 1 bar) equilibration with/without the main chain restrained for a total of 200 ps. Finally, the system was submitted to a 100-ns NPT (T = 300 K, p = 1 bar) production MD simulation by using the *pmemd.cuda* module. The *MMPBSA.py* module was used to calculate the binding free energy (ΔGbind) between hepcidin and FPN by using the MM/GBSA approach based

on 2000 snapshots extracted from the last 20-ns trajectories, and ΔGbind was further decomposed into the contributions of each residue in hepcidin.[30]

All-atomic MD simulation was also employed to investigate the dynamic processes of the self-assembly behavior of cholesterylated minihepcidin in solution. Briefly, the chemical structure of cholesterylated minihepcidin was created by Chem3D and was then optimized, and the partial atomic charges were calculated by the AM1-BCC method using the *Antechamber* module of Amber 20.[31] Ten molecules of cholesterylated minihepcidin were packed randomly by PACKMOL in a cubic box with a length of 60 Å. The molecular mechanics parameters from the GAFF force field were assigned to the packed system, which was subsequently neutralized by adding sodium/chlorine counter ions; then, the system was solvated in a cuboid box of transferable interatomic potential with three points model (TIP3P) water molecules with solvent layers 10.0 Å between solute surface and box edges, by using the LEaP module of Amber 20 [28,29]. The SHAKE algorithm was employed to restrict all covalent bonds involving hydrogen atoms. The *pmemd.MPI* module was used to perform the minimization, heat, density and equilibration. Two steps of minimization were performed, containing a main chain-restrained minimization with 50 kcal/(mol·Å^2) and a 10000-cycle nonrestrained minimization. The system was then heated from 0 K to 300 K in 80 ps and maintained at 300 K for 20 ps with a harmonic restraint of 10 kcal/(mol·Å^2) using Langevin dynamics at a constant volume, with a time step of 2 fs. Then, 100 ps of density equilibration was applied to the system, which subsequently underwent two steps of NPT (T = 300 K, p = 1 bar) equilibration with/without the main chain restrained for a total of 400 ps. Finally, the system was submitted to a 200-ns NPT (T = 300 K, p = 1 bar) production MD simulation by using the *pmemd.cuda* module. Chimera-1.15 was used to visualize the MD trajectories.[32] The conformations were visualized by PyMOL.

Histopathological analysis

Mouse lung tissues were fixed and embedded in paraffin wax. Lung sections (4 μm) were stained with hematoxylin and eosin (H&E) and observed under an Olympus VS120 microscope (Olympus, Tokyo, Japan). Histological lung injury was assessed and scored on a 5-point scale: 0, minimal damage; 1 to 2, mild damage; 2 to 3, moderate damage; 3 to 4, severe damage; and 4 +, maximal damage. Two examiners performed histopathological analysis without prior knowledge of the experimental interventions. The composition of collagen in lung tissues was stained with Picrosirius Red and observed by a Polarizing Optical Microscope with Heating Stage (Nikon, Japan).

In vivo lung permeability assay

Lung permeability was measured by Evans blue dye (EBD) leakage.[34,35] EBD (20 mg/kg, Sigma–Aldrich, E2129) in a 100 μL volume was administered intravenously through the tail vein 1h before euthanasia. Lungs were then perfused with normal saline through the right ventricle to remove intravascular dye. Then, the lungs were harvested and dried at 60°C for 48 h and incubated in formamide (Sigma–Aldrich, F9037) at 37°C for 24 h. Supernatants were collected after centrifugation at 5000 × g for 30 min. EBD in the supernatant was measured by a spectrophotometric method (wavelength 620 and 740 nm). The extravasation of EBD into lung tissue was calculated against a standard curve and expressed as the dye incorporated per mg of tissue.

Immunofluorescence staining

Frozen sections (8 μm) from isolated lungs were permeabilized with 0.25% Triton X-100, blocked with 3% BSA in PBS, and then stained with anti-alpha smooth muscle actin antibody (Abcam, ab7817) for 24hat 4°C. After washing with PBST (PBS containing 0.025% Tween 20) three times, sections were stained with goat anti-rabbit IgG and Alexa Fluor 488 (ThermoFisher, A-10680) for 1hat room temperature. All antibodies were diluted in blocking buffer. Images were captured by using an Olympus VS120 microscope (Olympus, Tokyo, Japan).

Lung epithelial proliferation assay

To assess lung epithelial cell proliferation, a distal lung digestion protocol was described as follows.[34,36] Briefly, the lungs were perfused with 10 mL PBS through the right ventricle of the heart and then filled with 1 mL RPMI medium with Liberase TM (50 μg/mL final concentration, Roche, 5401127001) and digested in 2 mL RPMI digestion medium for 30minat 37°C with vortexing every 10 min. To obtain a single cell suspension for fluorescent antibody staining by flow cytometry, cells were collected and passed through 100- and 70-μm strainers sequentially. Then, we devised a flow cytometry strategy (Figure S19) that utilized a BrdU pulse at 24 h

prior to euthanasia, followed by the identification of $CD45^-$, $EpCAM^+$ and $BrdU^+$ cells using flow cytometry. For lung epithelial cell sorting, total lung cells were stained with anti-CD45 antibody (eBioscience, 56-0451-82) and anti-mouse CD326 (Ep-CAM) antibody (BioLegend, 118207). BrdU staining was performed with BrdU flow kits from Biolegend following the manufacturer's protocol (BioLegend, 339812).

Murine macrophage isolation and culture

Pulmonary macrophages were isolated from mice by adhering bronchoalveolar lavage. In detail, the mice were disinfected with alcohol cotton balls on the neck and abdomen after anesthesia. Then, a small incision was made in the neck to expose the trachea. An 18 g needle was inserted into the trachea (just below the larynx) and tied tightly with surgical thread. A 1 mL syringe was used to slowly inject 0.5 mL of sterile PBS, gently massage the lung, gently pull back and push the syringe plunger 3 times to remove the cell suspension and collect it in a 15 mL tube containing the cell suspension. Thisstep was repeated 2 times. The cell suspension was centrifuged at 350×g for 5minat 4°C. The cells were resuspended in RPMI1640 containing 10% FBS, placed in a humidified incubator with 5% CO_2 and incubated at 37°C for 1 h. Unadhered cells were gently rinsed with PBS, and the adherent cells were harvested for further experiments.

The murine bone marrow-derived macrophages (BMDMs) were isolated as follows.[37] Briefly, bone marrow cells were isolated from mouse hind legs in a single cell suspension. After erythrocyte lysis, cells were resuspended in Dulbecco's modified Eagle's medium (DMEM) supplemented with 10% fetal bovine serum and 10 ng/mL granulocyte-macrophage colony stimulating factor (GM-CSF) in 75-cm^2 flasks and were maintained in a humidified incubator (Thermo Fisher Scientific, Rockford, IL) with 5% CO_2 at 37°C. Twenty-four hours later, the nonadherent cells were collected and replaced on 6-well culture plates, which were incubated for 7 days with medium exchange every 3 days.

Western blot

Pulmonary macrophages or BMDMs were isolated as described above. Then, the samples were lysed in RIPA buffer (Beyotime Biotechnology). Protein levels were determined using the BCA Protein Assay kit (Thermo Scientific). Equal amounts of total proteins from samples (20 μg or 40 μg) were separated by 12% sodium dodecyl sulfate–polyacrylamide gel electrophoresis (SDS–PAGE), transferred to polyvinylidene fluoride membranes (Millipore, Billerica, MA, USA), and detected via Western blot analysis. The primary antibodies used in the study included the following: anti-mouse ferroportin antibody (1:1000; Alpha Diagnostic International, MTP11-A), anti-alpha smooth muscle actin antibody (1:1000; Huabio, ET1607-43), anti-Areg antibody (1:1000; absin, abs115815), anti-EGFR antibody (1:1000; Abcam, ab52894), anti-EGFR (phospho Y1068) antibody [EP774Y] (1:1000; Abcam, ab40815), anti-YAP antibody (1:1000; Cell Signaling Technology, 14074), anti-phospho-YAP antibody (1:1000; Cell Signaling Technology, 13008), and anti-β-actin (1:5000; Sigma, A5441). After washing, the membranes were incubated with secondary antibodies conjugated to horseradish peroxidase. HRP-conjugated goat anti-rabbit IgG (H+L) (1:5000; MultiSciences, GAR0072) and HRP-conjugated goat anti-mouse IgG (H+L) (1:5000; MultiSciences, GAM0072) were used as secondary antibodies. The signals were detected via enzyme-linked chemiluminescence using the EZ-ECL kit (Biological Industries, Kibbutz Beit-Haemek, Israel).

Iron determination

Pulmonary macrophages were isolated as described above. Then, the pulmonary macrophages were lysed in extracting solution (Solarbio, BC4355) and centrifuged at 4000 × g for 10minat 4°C, and the supernatant was collected. BALF samples were collected from the experimental mice and centrifuged at 800 × g for 5 min. The cell-free supernatants were collected. Iron levels in pulmonary macrophages and BALF samples were measured by atomic absorption spectroscopy.[8]

Statistical analysis

All data are presented as the mean ± standard error of the mean (SEM). Statistical analyses were performed by using GraphPad Prism (version 8.0) software (GraphPad Software Inc., San Diego, CA, USA). For comparison between two experimental groups, unpaired two-tailed Student's t test or nonparametric test was performed. For more than two experimental groups, a one-way analysis of variance (ANOVA) was performed for comparison. Correlation analyses were performed by the pearson correlation method. For EC50 values, nonlinear regression [agonist] versus response was performed. In all cases, $p< 0.05$ was considered statistically significant. *$p< 0.05$; **$p< 0.01$; ***$p< 0.001$; ***$p< 0.0001$.